Available online at www.sciencedirect.com

ScienceDirect

Geochimica et Cosmochimica Acta 274 (2020) 302–316

Geochimica et Cosmochimica Acta

www.elsevier.com/locate/gca

Carbon and nutrient export from intertidal sand systems elucidated by $^{224}Ra/^{228}Th$ disequilibria

Pinghe Cai [a,b,*], Lin Wei [a,b], Walter Geibert [c], Dennis Koehler [c], Ying Ye [c], Wei Liu [a,b], Xiangming Shi [a,b]

[a] State Key Laboratory of Marine Environmental Science, Xiamen University, Xiamen 361005, PR China
[b] College of Ocean and Earth Sciences, Xiamen University, Xiamen 361005, PR China
[c] Alfred-Wegener Institute, Helmholtz Centre for Polar and Marine Research, Bremerhaven 27570, Germany

Received 18 November 2019; accepted in revised form 6 February 2020; Available online 14 February 2020

Abstract

We propose an alternative scheme for the use of $^{224}Ra/^{228}Th$ disequilibria to investigate carbon and nutrient export from a permeable sandy seabed. Sediment profiles of dissolved ^{224}Ra, total ^{224}Ra and ^{228}Th were determined at two different intertidal sand systems - an intertidal sandy beach near Weitou Bay in Fujian (China), and a tidal sand flat in the Wadden Sea near Cuxhaven (Germany). Dramatic deficit of total ^{224}Ra relative to ^{228}Th was identified in the upper 20 or 30 cm sand layer over the sand systems. We construct a simple two-dimensional advective cycling model to simulate interfacial fluid transport in a sand system that is subject to periodic tidal inundation and swash actions. Based on the $^{224}Ra/^{228}Th$ disequilibria in the sediment, the model gives estimates of 20.3, 9.1, and 1.9 L m^{-2} h^{-1} for water exchange flux at the high tide, mid-tide, and low tide position over the sandy beach at Weitou Bay, respectively. In comparison, the model provides an estimate of 7.2 L m^{-2} h^{-1} for water exchange flux at the tidal sand flat in the Wadden Sea.

The production of dissolved inorganic carbon (DIC) in porewater is the rate-limiting step for DIC export from the sandy beach into the sea, and can be reasonably simulated as a first-order kinetic reaction. The pattern of interfacial fluid transport over the beach facilitates a horizontal zonation of redox condition in the sediment, which evolves progressively from a fully oxic state at the high tide position to a suboxic state at the low tide position. There is clear evidence of nitrogen loss via denitrification in the suboxic status, and we estimate a nitrogen removal rate of 3.3 mmolN m^{-2} d^{-1} at this site. For the two intertidal sand systems, DIC export fluxes range from 20.1 to 89.4 mmolC m^{-2} d^{-1}, comparable in magnitude to fluxes determined in organic rich estuarine sediments. In the meantime, export fluxes of dissolved inorganic nitrogen (DIN) change from 0.8 to 18.6 mmolN m^{-2} d^{-1}. Overall, this study suggests that the role of sandy sediments in the biogeochemical cycling of carbon and nutrients needs to be revisited.

Keywords: Intertidal sandy beach; Porewater exchange; Dissolved inorganic carbon; Nutrients; Export flux; $^{224}Ra/^{228}Th$ disequilibria

1. INTRODUCTION

Permeable sediments are typically defined as sediments with a permeability greater than $\sim 10^{-12}$ to 10^{-11} m^2. Above this threshold, advective transport surpasses Brownian molecular diffusion and becomes the dominant process for solute exchange across the sediment-water interface (Huettel et al. 2014). Advective fluid transport in the upper

* Corresponding author at: State Key Laboratory of Marine Environmental Science, Xiamen University, Xiamen 361005, PR China.
E-mail address: Caiph@xmu.edu.cn (P. Cai).

https://doi.org/10.1016/j.gca.2020.02.007
0016-7037/

sediment layer is driven by pressure gradients at the sediment-water interface that are set up by a diversity of mechanisms, like tidal and wave pumping, wave setup, bottom current-topography interactions, and bio-irrigation (Santos et al., 2012). In the highly dynamic coastal ocean, benthic solute fluxes from permeable sediments induced by advective transport can exceed molecular diffusive fluxes by several orders of magnitude (Huettel et al., 2014; Cook et al., 2018).

Although highly permeable sandy sediments cover >40% of coastal and continental shelves worldwide (e.g., Riedl et al., 1972), biogeochemical reaction rates therein were traditionally thought to be low because of their low organic carbon contents. This viewpoint, however, has been challenged in the last decade (Anschutz et al. 2009). A number of investigators suggested that sandy sediments are biogeochemically highly active, and possess chemical remineralization rates comparable to organic rich muds (Berg et al., 2013). Advective transport processes of solutes and fine particles at the sediment-water interface were thought to facilitate fast recycling of organic matter, thereby converting permeable sand beds into efficient biocatalytical filters (Huettel et al., 1996, 1998). As such, low organic carbon contents may not necessarily be interpreted as an indicator of low metabolic activity in these environments, but rather a consequence of rapid turnover and exchange rates.

Despite the critical role of sandy sediments in coastal biogeochemistry, advective fluxes of water and solutes from permeable sand beds remain poorly constrained (e.g., Cook et al., 2018; Tamborski et al., 2019). Recently, a $^{224}Ra/^{228}$-Th disequilibrium method was developed to quantify benthic solute fluxes from coastal sediments (e.g., Cai et al., 2014, 2015). Simply, low activities of dissolvable ^{224}Ra in the near-surface sediment relative to its highly particle-reactive parent ^{228}Th (half-life = 1.91 a) indicate loss via solute transport across the sediment-water interface. As ^{224}Ra has a half-life of 3.66 days, this isotope pair is particularly suited to trace interfacial transport processes that occur over a time scale of 1–10 days. The $^{224}Ra/^{228}Th$ disequilibrium method is unique in that it does not introduce any artificial interference to the system. In previous studies, however, its application was limited mainly in muddy, cohesive sediments where interfacial solute exchange is dominated by irrigation (e.g., Aller, 1980). In this work, we expand the $^{224}Ra/^{228}Th$ disequilibrium method to examine carbon and nutrient export from intertidal sand systems, where advective transport is expected to dominate water and solute exchange across the sediment-water interface.

2. METHODS

2.1. Study sites and sample collection

Our sampling campaigns took place at two separate intertidal sand systems - an intertidal sandy beach near Weitou Bay in Fujian (China), and a tidal sand flat in the Wadden Sea near Cuxhaven (Germany). The intertidal sandy beach at Weitou Bay (24°31.33′N, 118°34.53′E) can be classified as an intermediate beach (Fig. 1). It is wide, of relatively low slope ($\tan\beta = 0.03–0.05$), and is fronted by an extensive surf zone where waves dissipate most of their energy before reaching the shoreline. Nonetheless, the beach is dominated by coarse-grained, highly permeable sands with an average porosity of ~0.4. During low tide, the surface sediment at the beach is unsaturated. Tides in the adjacent coastal sea are semidiurnal, and the tide range is typically 2–3 m.

In November 2017, sediment and porewater samples were collected at three different sites, i.e., WTW-H, -M, and -L, along a transect across the beach near Weitou Bay (Fig. 1). More specifically, WTW-H is located near the high tide line, WTW-M near the mid-tide line, and WTW-L slightly above the low tide line. Sediment cores were retrieved by forcing manually a PVC tube (inner diameter: 47 mm) into the sediment. Seawater samples were collected using a small submersible pump. Porewater samples (~3–5 liters) for ^{224}Ra analyses were collected at depths of 0–5, 5–10, 10–15, 15–20, 25–30, 45–50 cm below the sediment-water interface by use of drive-point piezometers and a peristaltic pump. Subsamples for salinity, dissolved inorganic carbon (DIC) and major nutrients were filtered through a 0.45 μm polycarbonate filter and were stored until analyses.

In order to assess the steady-state assumption for ^{224}Ra distributions in the sediment within an intertidal sand system, separate sediment cores were collected at a tidal sand flat in the German Wadden Sea (Fig. 1) by means of an acrylic glass tube (inner diameter: 62 mm) with pre-drilled holes for Rhizon sampling of porewater. The tidal flat that we investigated is dominated by mixed sand and silt with porosities of typically 0.3. During low tide, it is exposed to the atmosphere for about 4 h twice per day (8 h/day), and the surface sediment becomes unsaturated. The tidal range is typically 3.5 m. The average slopes are generally very small (approximately 1 m/500 m), but the sampling region is incised by channels that locally create steeper outflows. In addition, ripples may form cm-scale slopes. Over a 12-day period in September 2017, three replicate sediment cores were retrieved during low tide from a time-series station (53°50.88´N, 8°34.485´E) at the tidal flat. A moderate storm attacked this region the day before sampling. Although time-series measurements were only limited to surface-exchangeable ^{224}Ra and ^{228}Th in the sediment, seawater and porewater samples were collected during the first core sampling. Seawater samples were collected in large carboys. Porewater samples for ^{224}Ra and nutrient analyses were extracted at various sediment depths using Rhizon samplers. Radiochemical assay and nutrient analyses for the samples collected from the tidal sand flat were carried out in Alfred-Wegener Institute for Polar and Marine Research, Germany.

2.2. Radiochemical assay

Upon return to the lab, the sediment cores were sectioned into 1-cm thick slices that have a typical mass range of 40–60 grams (dry mass). Activities of surface-exchangeable ^{224}Ra and ^{228}Th in the sediment (hereafter simply refer to as total ^{224}Ra and ^{228}Th) were determined

Fig. 1. The sampling locations over an intertidal sandy beach at Weitou Bay (upper panel) and at a tidal sand flat in the German Wadden Sea near Cuxhaven (lower panel).

using a Radium Delayed Coincidence Counter (i.e., the RaDeCC system) as per Cai et al. (2012). For each sediment sample, three measurements were performed on a same RaDeCC counter in ~6–12 h, 10–12 days, and 3 weeks after sample collection, respectively. This procedure allows to deduce ^{224}Ra and ^{228}Th activities from the first and the second measurements, or from the first and the third measurements. By comparing the second and the third measurements, it also allows to assess the performance of the RaDeCC system (e.g., Cai et al., 2015). Because large grains tend to have a small surface area, surface-exchangeable ^{224}Ra and ^{228}Th activities in coarse, sandy sediment samples are expected to be low. As such, we increased counting time in the measurement to ~16 h so as to achieve a minimum of 1000 counts in the 220 channel. Chance coincidence and contributions from the 219 channel were corrected in a way detailed in Moore and Arnold (1996). The RaDeCC counter was calibrated with a ^{232}U-^{228}Th standard using the method of standard addition. All ^{224}Ra and ^{228}Th data were decay-corrected to the time of sample collection. The propagated error associated with ^{224}Ra and ^{228}Th activities in bulk sediment averages ~3–4% for the entire data set (Tables 1 and 2). A comparison of ^{228}Th activities computed from the first and the second measurements, and from the first and the third measurements gives a mean ratio of 1.004, and a relative

standard deviation of 5.3% (n = 55). Therefore, we conclude that the uncertainty on the reported ^{224}Ra and ^{228}Th data sets was properly assessed.

Seawater and porewater samples for ^{224}Ra analyses were pre-filtered through a 142 mm 0.7 μm (nominal pore size) GFF filter to remove suspended particles. Seawater filtrates were passed through a column of MnO_2-impregnated fiber at a flow rate of <0.5 L min^{-1}. The fiber was partially dried, and ^{224}Ra absorbed thereon was measured on a RaDeCC counter according to the classic procedure detailed in Moore and Arnold (1996). Porewater ^{224}Ra was co-precipitated onto MnO_2 suspension by adding a certain amount of $KMnO_4$ and $MnCl_2$ solutions into the sample. The MnO_2 suspension was filtered onto a GFF filter, which was then counted in a RaDeCC system. The counting efficiency was determined using a ^{232}U-^{228}Th standard prepared in the same manner as the aqueous samples.

2.3. Other elemental analyses

Salinity of the seawater and porewater samples collected from the intertidal sandy beach at Weitou Bay was measured by use of a salinometer (Wissenschaftlich-Technische Werkstätten GmbH Multi 340i). DIC was determined within 24 h after sample collection via acidification of the sample and subsequent quantification of CO_2 with an infrared analyzer (Cai et al., 2004). Ammonium (NH_4^+) was measured upon return to the lab as per the indophenol blue spectrophotometric method (Dai et al., 2008). Quantification of nitrate (NO_3^-) and nitrite (NO_2^-) was based on the classical colorimetric method by use of a Four-channel Continuous Flow Technicon AA3 Auto-Analyzer (Bran-Lube GmbH). The detection limits for NO_3^-, NO_2^-, and NH_4^+ were 0.07, 0.02, and 0.16 μM, respectively. Seawater and porewater NH_4^+ concentrations in this setting, however, were below the detection limit. As such, we report only the sum of nitrate and nitrite, and hereafter simply refer to it as NO_3^-. Total organic carbon (TOC) content in the sediment was determined using a CHN elemental analyzer (Thermo Delta V Advantage & Elementar vario EL CUBE). All samples were pretreated with 0.1 M HCl solution to remove $CaCO_3$. Grain size analysis was performed with a laser particle analyzer (Malvern 3000).

For the tidal sand flat in the German Wadden Sea, we only measured the concentration of major nutrients in porewater, using a QuAAtro Continuous Segmented Flow Analyzer (Seal Analytical) in 1:10 dilution. Duplicate analyses all agreed within 2% (NO_x), 6.3% (PO_4^{3-}), and 9% (Si). The analysis of reference material CJ (KANSO) was found to agree within 2.5% of the certified value for all reported species.

3. RESULTS

Activities of total ^{224}Ra and ^{228}Th in the sediment as well as grain size and TOC content from the sandy beach at Weitou Bay are presented in Table 1. Measurements of ^{224}Ra and ^{228}Th activities from the tidal flat sediment at the time-series station in the German Wadden Sea are shown in Table 2. Activities of ^{224}Ra, salinity, temperature, DIC, and NO_3^- in the dissolved phase (porewater and seawater) for the intertidal sandy beach at Weitou Bay are listed in Table 3. Activities of ^{224}Ra as well as major nutrients in porewater and seawater for the tidal sand flat in the German Wadden Se are presented in Table 4. During the survey, temperature in the surface seawater and in the upper 0–50 cm sediment porewater at Weitou Bay changed from 18.4 °C to 24.0 °C. Salinity in the porewater and in the surface seawater was similar, falling in a narrow range of 30.2–32.5. Porewater profiles of salinity were relatively uniform, and did not show clear evidence of fresh groundwater input into the system (Table 3).

3.1. Total ^{224}Ra and ^{228}Th in the sediment

Depth profiles of total ^{224}Ra and ^{228}Th in the upper 0–35 cm sediment layer across the intertidal sandy beach at Weitou Bay are shown in Fig. 2. Total activities of ^{224}Ra in the sediment ranged from 0.023 to 0.072 dpm g^{-1}. In comparison, ^{228}Th activities in the sediment varied from 0.030 to 0.076 dpm g^{-1}, which is much lower than those measured in muddy sediments (e.g., Cai et al., 2014, 2015). This could be a result of the difference in grain size and sediment mineralogy between the two types of sediment. Indeed, depth profiles of total ^{224}Ra and ^{228}Th show highs and lows, which were in concert with the peaks and troughs of grain size in the sediment (Lower panel, Fig. 2).

A prominent feature shown in Fig. 2 is that total ^{224}Ra was in dramatic deficit with respect to ^{228}Th in the sediment. The activity ratio of total ^{224}Ra to ^{228}Th was generally lower than 0.80 in the upper 0–20 cm sediment layer, and at the sampling site close to the low tide line (WTW-L), it was as low as ~0.50 in the upper 0–2 cm sediment layer (Table 1). The total ^{224}Ra/^{228}Th ratios in this system are significantly lower than those observed in muddy sediments (e.g., Cai et al., 2015; Hong et al., 2017; Shi et al., 2019). In addition, the penetration of ^{224}Ra deficit in the sediment can be down to a depth of >30 cm at St. WTW-M, much deeper than that observed in muddy sediments (~10 cm). Overall, it indicates that intertidal sandy beaches are characterized by much more intense interfacial fluid exchange than in muddy sediment systems.

Like the intertidal sandy beach at Weitou Bay, depth distributions of total ^{224}Ra and ^{228}Th at the tidal sand flat in the German Wadden Sea exhibited large deficit of ^{224}Ra in the sediment column (Fig. 3). The activity ratio of total ^{224}Ra to ^{228}Th varied from a low of 0.43 to a high of 1.10 in the upper 0–20 cm sediment layer (Table 2). In addition, total ^{224}Ra did not reach secular equilibrium with ^{228}Th at the sampling depth. Notably, total ^{224}Ra and ^{228}Th activities in the sediment at this location are significantly higher compared to the intertidal sandy beach at Weitou Bay, possibly reflecting the difference in grain size and sediment mineralogy between the two separate regions.

3.2. Porewater constituents and TOC

Activities of dissolved ^{224}Ra in porewater for the intertidal sandy beach at Weitou Bay varied in a relatively narrow range, from 6.4 to 16.4 dpm l^{-1} (Fig. 4). In

Table 1
Grain size, TOC content, as well as total ^{224}Ra and ^{228}Th activities in the sand over an intertidal beach near Weitou Bay in Fujian, China.

Depth (cm)	Grain size (φ)	TOC (wt%)	$^{224}Ra_T$ (dpm g^{-1})	^{228}Th (dpm g^{-1})	^{224}Ra/^{228}Th (A.R.)
Station: WTW-H					
0-1	1.8	0.038	0.033 ± 0.001	0.050 ± 0.001	0.66 ± 0.03
1-2	1.5	0.028	0.034 ± 0.001	0.059 ± 0.001	0.58 ± 0.03
2-3	1.7	0.021	0.040 ± 0.001	0.055 ± 0.001	0.73 ± 0.03
3-4	1.7	0.027	0.030 ± 0.001	0.047 ± 0.001	0.62 ± 0.03
4-5	1.5	0.029	0.037 ± 0.001	0.052 ± 0.001	0.72 ± 0.03
9-10	1.0	0.025	0.028 ± 0.001	0.036 ± 0.001	0.78 ± 0.04
14-15	1.5	0.032	0.041 ± 0.001	0.053 ± 0.001	0.78 ± 0.03
19-20	1.7	0.024	0.044 ± 0.001	0.054 ± 0.001	0.80 ± 0.03
24-25	1.1	0.023	0.052 ± 0.001	0.052 ± 0.001	0.99 ± 0.03
29-30	0.7	0.036	0.033 ± 0.001	0.030 ± 0.001	1.10 ± 0.05
Station: WTW-M					
0-1	1.4	0.037	0.029 ± 0.001	0.050 ± 0.001	0.58 ± 0.03
1-2	1.5	0.028	0.031 ± 0.001	0.050 ± 0.001	0.61 ± 0.03
2-3	1.7	0.041	0.031 ± 0.001	0.049 ± 0.001	0.64 ± 0.03
3-4	1.0	0.030	0.023 ± 0.001	0.038 ± 0.001	0.61 ± 0.03
4-5	0.9	0.032	0.024 ± 0.001	0.033 ± 0.001	0.75 ± 0.04
9-10	0.7	0.033	0.029 ± 0.001	0.043 ± 0.001	0.68 ± 0.03
14-15	0.6	0.028	0.028 ± 0.001	0.037 ± 0.001	0.78 ± 0.04
19-20	0.1	0.035	0.023 ± 0.001	0.036 ± 0.001	0.64 ± 0.03
24-25	0.2	0.026	0.028 ± 0.001	0.033 ± 0.001	0.86 ± 0.04
29-30	0.7	0.026	0.034 ± 0.001	0.038 ± 0.001	0.89 ± 0.04
34-35	1.6	0.033	0.058 ± 0.002	0.062 ± 0.001	0.93 ± 0.04
Station: WTW-L					
0-1	0.8	0.032	0.026 ± 0.001	0.049 ± 0.001	0.54 ± 0.03
1-2	0.5	0.034	0.026 ± 0.001	0.048 ± 0.001	0.53 ± 0.03
2-3	0.6	0.048	0.034 ± 0.001	0.053 ± 0.001	0.65 ± 0.03
3-4	0.9	0.064	0.047 ± 0.002	0.065 ± 0.001	0.71 ± 0.03
4-5	0.9	0.069	0.051 ± 0.002	0.076 ± 0.001	0.68 ± 0.03
9-10	0.8	0.034	0.072 ± 0.002	0.073 ± 0.001	0.99 ± 0.04
14-15	0.1	0.045	0.034 ± 0.001	0.038 ± 0.001	0.89 ± 0.04
19-20	0.1	0.024	0.040 ± 0.002	0.042 ± 0.001	0.95 ± 0.04
24-25	0.3	0.023	0.067 ± 0.002	0.062 ± 0.001	1.08 ± 0.04
30-31	1.1	0.028	0.071 ± 0.002	0.069 ± 0.001	1.03 ± 0.04

comparison, activities of ^{224}Ra in seawater were much lower, ranging from ~0.6 to 0.8 dpm l^{-1}. DIC concentrations in porewater fell in the range of 2237–3135 μM, compared to a level of ~2100 μM in seawater. Interestingly, there was a clear trend of seaward increase in porewater DIC concentration over the beach (Fig. 4). Nitrate (NO_3^-+NO_2^-) concentrations in porewater changed from 42.5 to 163 μM, considerably higher than a concentration level of ~24 μM in seawater. In addition, porewater nitrate profiles exhibited a horizontal zonation with maximum concentrations occurring at the site near the mid-tide line, i.e., at WTW-M. TOC content in the sandy sediment was low, ranging from 0.021% to 0.069% (wt%, see Table 1).

A single depth profile collected from the tidal sand flat in the German Wadden Sea showed that porewater ^{224}Ra activities at this location changed from 9.8 to 28.3 dpm l^{-1}, much higher than the activity of 2.3 dpm l^{-1} in seawater (Table 4). Nitrate (NO_3^-+NO_2^-) concentrations in porewater varied between 20 and 226 μM. NH_4^+ concentrations in porewater were relatively uniform, ranging from 62 to 73 μM. In comparison, PO_4^{3-} concentrations in porewater were much lower, changing from 1.9 to 5.9 μM (Table 4).

4. DISCUSSION

4.1. Interfacial transport models

4.1.1. Radium-224 deficit model

In marine sediments, ^{224}Ra is continuously produced via alpha decay of ^{228}Th that is strongly bound to solid particles. As radium is dissolvable in saline waters, a significant portion of ^{224}Ra originally resided in the solid phase will enter the interstitial water. By diffusion and advection, some ^{224}Ra may ultimately migrate across the sediment-water interface into the overlying water column, thereby resulting in deficit of ^{224}Ra relative to ^{228}Th in the near-surface sediment. The general expression that describes the rate of change in ^{224}Ra activity is given by

$$\frac{\partial A_{Ra}}{\partial t} = A_{Th}\lambda_{Ra} - A_{Ra}\lambda_{Ra} - \nabla F \quad (1)$$

where A_{Ra} and A_{Th} denote ^{224}Ra and ^{228}Th activities in wet sediment (dpm cm^{-3}); t is time; λ_{Ra} is the decay constant of ^{224}Ra (=0.189 d^{-1}); F is ^{224}Ra flux induced by fluid transport; ∇ is gradient operator in respective coordinate sys-

Table 2
Total ^{224}Ra and ^{228}Th activities in three replicate sediment cores (R1, R2, and R3) collected from a tidal sand flat (53°50.88′N, 8°34.485′E) in the German Wadden Sea.

Depth (cm)	Porosity	$^{224}Ra_T$ (dpm g^{-1})	^{228}Th (dpm g^{-1})	$^{224}Ra/^{228}Th$ (A.R.)
Time-series measurement: R1				
0-1	0.449	0.166 ± 0.006	0.151 ± 0.004	1.10 ± 0.05
1-2	0.457	0.109 ± 0.006	0.139 ± 0.003	0.79 ± 0.05
2-3	0.433	0.098 ± 0.005	0.221 ± 0.005	0.44 ± 0.02
3-4	0.408	0.113 ± 0.005	0.182 ± 0.004	0.62 ± 0.03
4-5	0.416	0.083 ± 0.006	0.192 ± 0.004	0.43 ± 0.03
9-10	0.444	0.084 ± 0.005	0.135 ± 0.004	0.62 ± 0.04
14-15	0.464	0.086 ± 0.005	0.117 ± 0.003	0.74 ± 0.04
19-20	0.444	0.083 ± 0.004	0.117 ± 0.003	0.71 ± 0.04
Time-series measurement: R2				
0-1	–	0.154 ± 0.007	0.204 ± 0.005	0.76 ± 0.04
1-2	–	0.114 ± 0.005	0.156 ± 0.004	0.73 ± 0.04
2-3	–	0.105 ± 0.004	0.142 ± 0.003	0.74 ± 0.03
3-4	–	0.103 ± 0.004	0.137 ± 0.003	0.75 ± 0.04
4-5	–	0.132 ± 0.007	0.201 ± 0.005	0.66 ± 0.04
9-10	–	0.088 ± 0.005	0.137 ± 0.004	0.64 ± 0.04
14-15	–	0.091 ± 0.004	0.117 ± 0.003	0.78 ± 0.04
19-20	–	0.107 ± 0.005	0.123 ± 0.003	0.87 ± 0.05
Time-series measurement: R3				
0-1	–	0.182 ± 0.007	0.236 ± 0.005	0.77 ± 0.03
1-2	–	0.128 ± 0.006	0.168 ± 0.004	0.76 ± 0.04
2-3	–	0.123 ± 0.005	0.157 ± 0.004	0.78 ± 0.04
3-4	–	0.117 ± 0.005	0.145 ± 0.003	0.80 ± 0.04
4-5	–	0.145 ± 0.007	0.210 ± 0.005	0.70 ± 0.04
9-10	–	0.108 ± 0.005	0.141 ± 0.003	0.76 ± 0.04
14-15	–	0.075 ± 0.004	0.114 ± 0.002	0.66 ± 0.04
19-20	–	0.088 ± 0.004	0.120 ± 0.003	0.73 ± 0.04

Table 3
Salinity (S), temperature (T), DIC, NO_3^-, and activities of ^{224}Ra in porewater and seawater collected from the sandy beach near Weitou Bay in Fujian, China.

Depth (cm)	S	T (°C)	DIC (μM)	NO_3^- (μM)	NO_2^- (μM)	$^{224}Ra_D$ (dpm L^{-1})
Station: WTW-H; Porosity = 0.40						
Seawater	32.0	24.0	2116	23.3	1.6	0.81 ± 0.03
0-5	30.2	23.1	2526	83.8	0.2	10.8 ± 0.3
5-10	30.7	22.8	2334	63.4	0.2	8.6 ± 0.3
10-15	30.6	22.8	2317	64.0	0.1	11.2 ± 0.3
15-20	30.7	22.8	2279	61.8	0.1	11.6 ± 0.3
25-30	30.6	22.7	2350	58.2	0.1	9.6 ± 0.3
45-50	30.5	23.5	2237	42.5	0.1	9.2 ± 0.2
Station: WTW-M; Porosity = 0.37						
Seawater	31.0	19.4	2103	23.8	0.9	0.59 ± 0.03
0-5	30.6	18.4	2688	134	0.3	8.1 ± 0.2
5-10	30.7	19.2	2735	135	0.2	10.2 ± 0.3
10-15	30.6	19.0	2674	150	0.0	9.5 ± 0.3
15-20	30.9	18.9	2654	163	0.0	13.6 ± 0.4
25-30	30.7	19.4	2602	145	0.0	9.4 ± 0.3
45-50	30.6	20.1	2561	118	0.0	7.5 ± 0.3
Station: WTW-L; Porosity = 0.40						
Seawater	31.2	22.7	2107	24.9	0.9	0.65 ± 0.03
0-5	32.5	22.1	2557	40.4	11.7	14.6 ± 0.4
5-10	32.4	22.4	2960	43.8	15.8	10.3 ± 0.3
10-15	32.5	22.2	3045	42.4	16.4	16.4 ± 0.5
15-20	32.5	22.4	3043	55.4	17.5	13.7 ± 0.4
25-30	32.4	22.9	3063	80.0	10.0	12.1 ± 0.4
45-50	31.8	23.1	3135	114	2.1	6.4 ± 0.2

Table 4
^{224}Ra activities and major nutrients in porewater and seawater collected during the first core measurement at the tidal sand flat in the Wadden Sea near Cuxhaven, Germany.

Depth (cm)	NO_3^- (μM)	NO_2^- (μM)	NH_4^+ (μM)	PO_4^{3-} (μM)	$Si(OH)_4$ (μM)	$^{224}Ra_D$ (dpm L^{-1})
Seawater	2.3	BD	BD	0.5	161	2.3 ± 0.09
0-1	226.1	0.35	69.4	5.9	59.7	9.8 ± 0.7
2-3	34.9	0.23	64.4	2.9	67.1	–
4-5	195.7	0.22	61.9	2.2	61.7	28.3 ± 1.5
6-7	175.0	0.21	65.2	2.2	80.3	–
8-9	29.7	0.21	69.4	1.9	103.8	–
10-11	20.0	0.22	73.2	3.0	95.8	–
12-13	223.1	0.16	73.3	3.8	121.2	–
14-15	169.2	0.24	73.0	4.1	121.3	–
16-17	196.1	0.17	71.9	3.8	134.3	–
18-19	9.4	0.16	70.3	3.1	109.8	–

BD: Below detection limit.

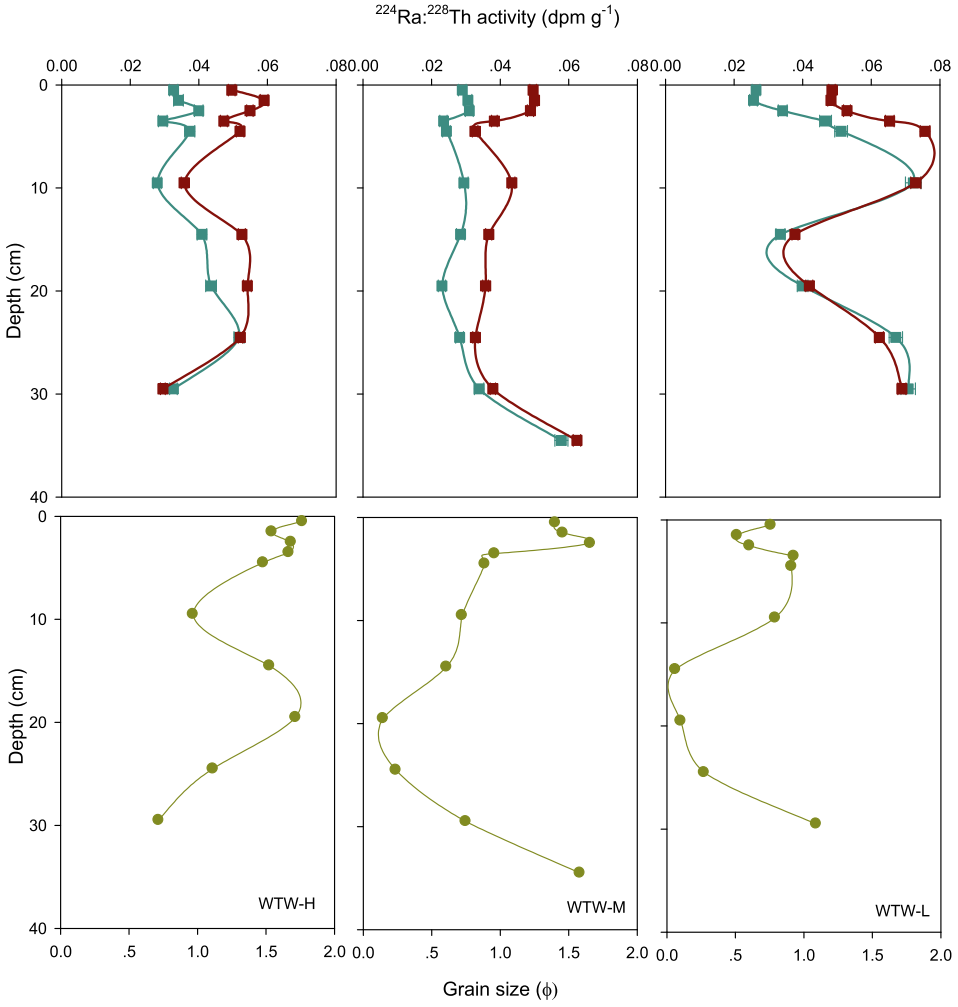

Fig. 2. Depth profiles of total ^{224}Ra (filled cyan square) and ^{228}Th (filled red square) in the 0–35 cm sand layer (upper panel), and the vertical patterns of grain size (lower panel) at the intertidal beach at Weitou Bay in Fujian, China. Error bars (±1σ) with ^{224}Ra and ^{228}Th data are shown only if larger than the symbol size.

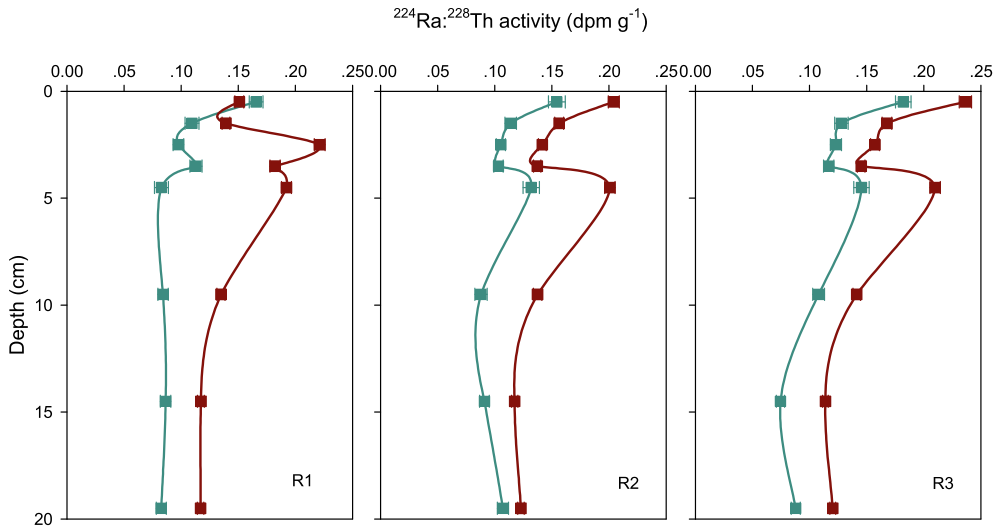

Fig. 3. Time-series measurements of total ^{224}Ra (filled cyan square) and ^{228}Th (filled red square) in three replicate sediment cores (R1, R2, and R3) collected from an intertidal flat in the German Wadden Sea. Error bars (±1σ) with ^{224}Ra and ^{228}Th data are shown only if larger than the symbol size. (For interpretation of the references to color in this figure legend, the reader is referred to the web version of this article.)

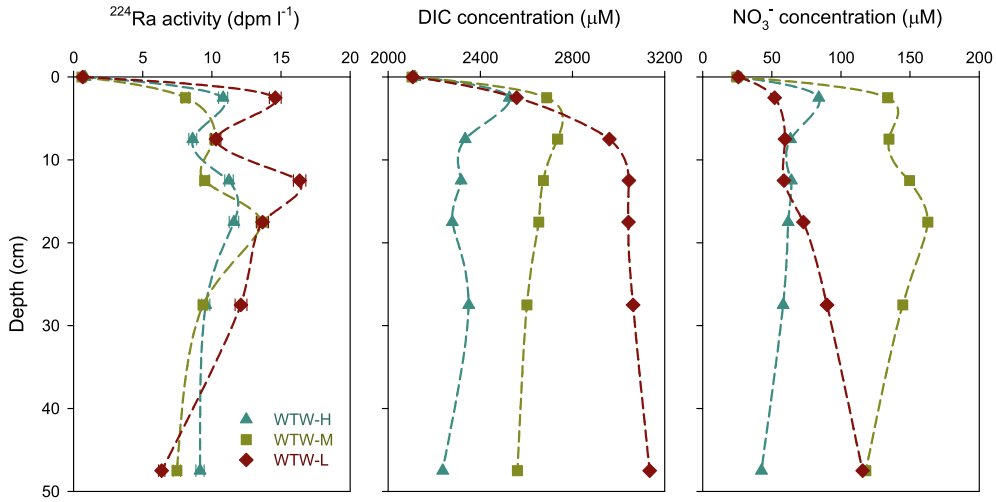

Fig. 4. Porewater profiles of ^{224}Ra, dissolved inorganic carbon (DIC), and NO_3^- (nitrate + nitrite) at different tidal positions over the intertidal sandy beach at Weitou Bay.

tem. In an intertidal sandy beach with a slope, both vertical and horizontal processes are expected to exert an effect on fluid transport across the sediment-water interface. If we assume that the beach surface is the main site for interfacial exchange of porewater and seawater, and that the distribution of ^{224}Ra in the sediment is at steady state, then flux of ^{224}Ra at any depth can be expressed as

$$F_{Ra} = \int_z^{\infty} \lambda_{Ra}(A_{Th} - A_{Ra})dz \quad (2)$$

Integrating ^{224}Ra deficit in the sediment from z = 0 to ∞ gives the net interfacial flux of ^{224}Ra out of the beach face.

4.1.2. Advective fluid transport model

Beaches are subject to wave actions in addition to tides. Interfacial fluid transport takes place when swashes run up the beach, cross the water table outcrop, and infiltrate into unsaturated sands. As soon as the backwash retreats, porewater drains out of the sands, and the water table outcrop moves backward again. This cycle will be repeated for every swash invasion and retreat. In the subtidal zone, interactions of wave-induced oscillatory flows and bottom topography (e.g., ripples) create pressure gradients over the seafloor that drive fluid exchange across the sediment-water interface. Interfacial fluid exchange through the seabed occurs also in response to wave pumping, i.e., it is driven by the pressure differences between wave crests and troughs passing overhead. As the frequency of waves and swashes on coastal beaches is nearly 10^3 times that of the tides, they represent a considerable amount of hydrodynamic energy and can be more important than tides as a mechanism that drives interfacial fluid transport.

In the subtidal sand bed, interfacial fluid transport has been well simulated using an advection cycling model (e.g., Cook et al., 2018). This model comprises a succession of vertically-stacked reservoirs. Water and solutes are assumed to be perfectly mixed within each reservoir, and only advective transport between the reservoirs is considered. Hydrodynamic dispersion is implicitly simulated through mixing within the reservoirs and not explicitly included in the governing equations. In essence, the model represents a two-dimensional recirculation cell, in which flow reverses periodically. By assuming that horizontal transit time is negligible, however, the two-dimensional model collapses into two one-dimensional compartments that exchange water and solutes. Each reservoir is assumed to continuously exchange water with the reservoirs immediately above and below, and also with the reservoir at the equivalent depth in the adjacent compartment. The downward flow in one compartment is balanced by the upward flux in the other compartment, and the horizontal flux between the two compartments is determined by the change in vertical water flux with depth (Cook et al., 2018).

We modify this advection cycling model to adapt to interfacial fluid transport in the intertidal sandy beach. Our modified model does not include an upward flux component. It consists of two phases: in the first phase when tides rise or when swashes run up the beach, seawater infiltrates into unsaturated sands and the beach acts solely as a water tank (Upper panel, Fig. 5); in the subsequent phase when tides fall or when swashes retreat, porewater drains out of the sand and the beach can be treated simply as a water supplier. During the drainage phase, porewater and solutes in each reservoir of the compartment are assumed to drain directly into the sea (Lower panel, Fig. 5). The downward flow in the compartment during the infiltration phase is balanced by the horizontal flow during the subsequent drainage phase. The change in vertical water flux with depth is related to the saturation state of the beach. In quasi steady-state, the distribution of total ^{224}Ra in wet sediment can be expressed as

$$\frac{\partial A_{Ra}}{\partial t} = \omega A^{0}_{DRa} + \lambda_{Ra} A_{Th} - \lambda_{Ra} A_{Ra} - s A_{DRa} \approx 0 \quad (3)$$

where A_{DRa} and A^{0}_{DRa} denote activity of dissolved ^{224}Ra in porewater and in seawater, respectively; ω and s represent seawater infiltration rate and porewater drainage rate in a unit volume of sediment (unit: $m^3\ m^{-3}\ d^{-1}$ or d^{-1}), respectively. Over the time scale that the ^{224}Ra/^{228}Th isotopic system integrates (1–10 d), there will be no net gain or loss of

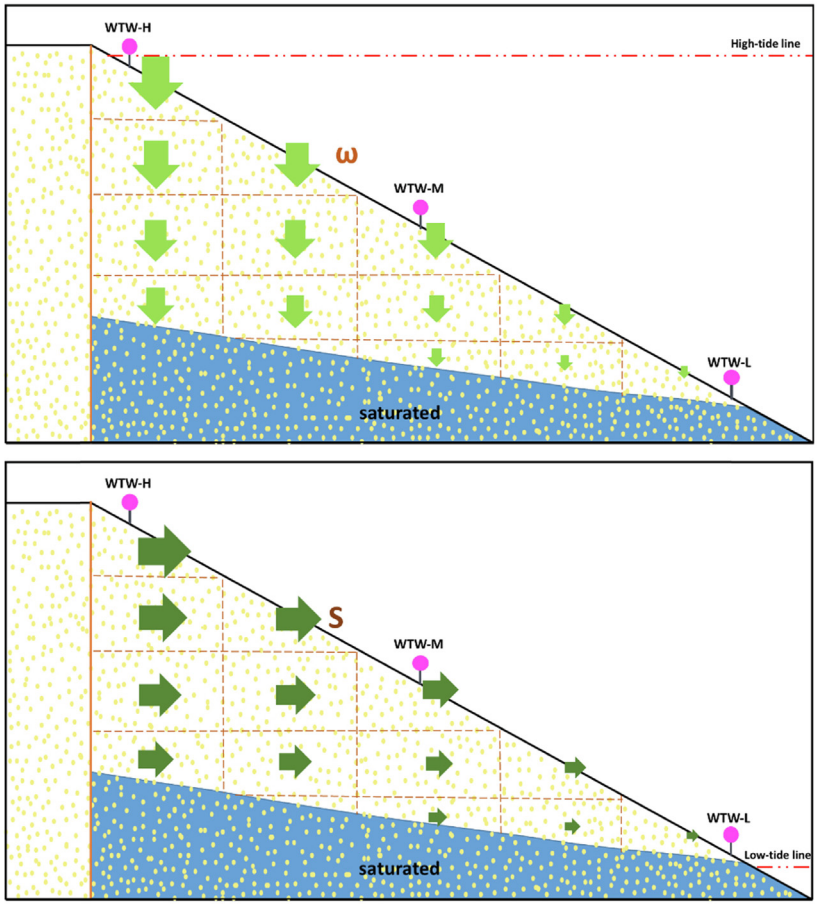

Fig. 5. A schematic of fluid transport within an intertidal sandy beach. The upper panel represents a seawater infiltration phase when tides rise, seawater infiltrates into the unsaturated sands; the lower panel depicts a subsequent porewater drainage phase when tides fall, porewater within the sandy beach drains into the sea.

mass for the entire beach. Therefore, seawater infiltration rate must be equal to porewater drainage rate, i.e., $\omega = s$. By reformulating Eq. (3) and integrating ^{224}Ra deficit in the sediment from z to ∞, we establish a relation of interfacial ^{224}Ra flux and seawater infiltration (or porewater drainage) rate:

$$F_{Ra} = \int_z^{\infty} \omega(A_{DRa} - A^0_{DRa})dz \quad (4)$$

Note that water exchange flux at any sand depth (W_z, unit: $m^3\ m^{-2}\ d^{-1}$ or $m\ d^{-1}$) can be expressed as

$$W_z = \int_z^{\infty} \omega dz \quad (5)$$

4.1.3. Steady-state assumption

For a sand system subject to tidal inundation, ^{224}Ra distributions in the upper sediment layer must not strictly be in steady state. As tides fall, seawater starts to retreat and the beach face may then be exposed. The beach face ultimately becomes unsaturated and fluid exchange across the sediment-water interface ceases. Under such a circumstance, ^{224}Ra in the unsaturated sediment layer will start to increase toward secular equilibrium with ^{228}Th. Conversely, when tides rise, seawater overtakes the beach face again, and interfacial fluid transport restarts. Radium-224 in the upper sediment layer turns around and decreases toward a level where gain of ^{224}Ra via production from ^{228}Th is balanced by loss of ^{224}Ra via decay and porewater exchange. However, given that the mean life of ^{224}Ra ($1/\lambda = 5.3$ d) is considerably longer than the period of tidal inundation ($T < 0.5$ d), such a type of high-frequency process would be smoothed out by the ^{224}Ra/^{228}Th system. As such, quasi steady-state for ^{224}Ra distribution in an intertidal sand system may be approximated, i.e., $\partial A_{Ra}/\partial t \approx 0$.

The time-series measurements of total ^{224}Ra and ^{228}Th from the tidal sand flat in the German Wadden Sea allow to test this steady-state assumption. As shown in Table 2, measurements of total ^{224}Ra for the time-series samples at any specific sediment depth generally agree within a relative standard deviation of ±20%. This level of agreement is fairly good, particularly when taking into account that some changes in the total ^{224}Ra activities may simply be caused by heterogeneity of the sediment, as manifested by the depth distributions of ^{228}Th (Fig. 3). When using Eq. (2) to integrate all ^{224}Ra deficit from the sediment surface to the sampling depth of 20 cm, we derive ^{224}Ra fluxes of 2850 ± 100, 2250 ± 110, and 2260 ± 100 dpm $m^{-2}\ d^{-1}$ for the time-series measurements at the tidal flat. The ^{224}Ra flux from the first core measurement is slightly higher than fluxes from the other two. This difference could be caused by the storm event that took place before the start of the sampling campaign and seemed to have been recorded by the first core measurement. Nonetheless, the three flux estimates are consistent within a relative standard deviation of ±20%. Therefore, we conclude that the quasi steady-state assumption for ^{224}Ra distribution in an intertidal sand system can be approximated.

4.2. Seawater infiltration rate and water exchange flux

When applying Eq. (2) to the intertidal sandy beach at Weitou Bay, we derive considerably lower ^{224}Ra fluxes into the sea of 800 ± 40, 1040 ± 40, and 500 ± 50 dpm $m^{-2}\ d^{-1}$ for WTW-H, WTW-M, and WTW-L, respectively. It should be noted that WTW-H, WTW-M, and WTW-L were located at a different tidal position in the sandy beach, which was inundated for ~2, 6, and 9 h during each tidal cycle. Because interfacial fluid transport takes place only when seawater interacts with beach sands, the above estimates correspond to ^{224}Ra fluxes of 200 ± 10, 87 ± 3, and 28 ± 3 dpm $m^{-2}\ h^{-1}$, respectively. Likewise, when taking into account the daily inundation time (~16 h), we obtain an equivalent ^{224}R flux of 153 ± 7 dpm $m^{-2}\ h^{-1}$ for the tidal sand flat in the German Wadden Sea (Table 5). As the deficit of ^{224}Ra in the sediment is a result of the sum of all processes that operate near the sediment-water interface, the total flux of ^{224}Ra also includes the component mediated by molecular diffusion. Based on the concentration gradients of dissolved ^{224}Ra across the sediment-water interface and by use of Fick's First Law (e.g., Cai et al., 2015), we estimate molecular diffusive ^{224}Ra fluxes of 0.8, 0.5, 1.1, and 3.1 dpm $m^{-2}\ h^{-1}$ for WTW-H, WTW-M, WTW-L, and the tidal sand flat in the German Wadden Sea, respectively. These estimates are two orders of magnitude lower than the total fluxes of ^{224}Ra, suggesting that advective flows govern interfacial fluid transport in the intertidal sand systems.

With measurements of ^{224}Ra deficit in the sediment and ^{224}Ra activities in the dissolved phase (porewater and seawater), we take advantage of Eq. (3) to estimate seawater

Table 5
^{224}Ra flux, seawater infiltration rate, water exchange flux, porewater residence time, DIC and DIN fluxes as well as TOC turnover time at different tidal positions over the intertidal sandy beach near Weitou Bay in Fujian (China) and at a tidal sand flat in the Wadden Sea (WDS) near Cuxhaven (Germany).

Station	^{224}Ra flux (dpm $m^{-2}\ h^{-1}$)	Seawater infiltration rate[a] (h^{-1})	Water flux (L $m^{-2}\ h^{-1}$)	Porewater residence time (h)	DIC flux (mmolC $m^{-2}\ d^{-1}$)	DIN flux (mmolN $m^{-2}\ d^{-1}$)	TOC turnover time (d)
WTW-H	200 ± 10	0–0.184 (0.086)	20.3 ± 1.1	5.9 ± 0.3	21.8 ± 1.0	3.6 ± 0.2	490
WTW-M	87 ± 3	0.012–0.071 (0.037)	9.1 ± 0.7	12.3 ± 0.5	65.9 ± 2.6	13.7 ± 0.6	220
WTW-L	28 ± 3	0–0.027 (0.012)	1.9 ± 0.3	62.6 ± 8.7	20.1 ± 4.4	0.8 ± 0.2	730
WDS	153 ± 7	0–0.129 (0.043)	7.2 ± 0.4	12.2 ± 0.7	89.4 ± 6.0	18.6 ± 1.2	–

[a] This column presents the range of seawater infiltration rate with the average value (in brackets).

infiltration/porewater drainage rate at any sediment depth. Our calculation shows that seawater infiltration rate changed essentially from zero to a maximum of 0.184 h^{-1} by taking into account the daily inundation time at different sampling sites. As opposed to porewater DIC concentration, there was a clear trend of seaward decrease in seawater infiltration rate over the intertidal sandy beach at Weitou Bay (see Table 5).

By assuming that seawater infiltration rate was zero below the sampling depth, we use Eq. (5) to calculate water exchange flux across the sediment-water interface. Interfacial water exchange fluxes were 20.3 ± 1.1, 9.1 ± 0.7, and 1.9 ± 0.3 L m^{-2} h^{-1} for WTW-H, WTW-M, and WTW-L, respectively (see Table 5). In comparison, interfacial water exchange flux was estimated to be 7.2 ± 0.4 L m^{-2} h^{-1} for the tidal sand flat in the German Wadden Sea. When taking into account the daily inundation time, these estimates are equivalent to interfacial water exchange fluxes of 81 ± 4, 109 ± 4, 35 ± 5, and 115 ± 6 L m^{-2} d^{-1}, respectively. Nonetheless, we should point out that the value of 115 ± 6 L m^{-2} d^{-1} must be regarded as a lower limit of the interfacial water exchange flux at the tidal sand flat in the German Wadden Sea because ^{224}Ra deficit relative to ^{228}Th in the sediment may still exist below the sampling depth (Fig. 3). The trend of seaward decrease in interfacial water exchange flux observed at the intertidal sandy beach near Weitou Bay is likely related to the saturation state of the beach at different tidal positions. The saturation state of sands varied both spatially within the beach and temporally through the tidal cycle. With height above the water table, surface sands at the high tide position in a beach are generally characterized by a larger saturation gap (i.e., the amount of air space in the sand), as compared to sands at the low tide position (McLachlan and Turner, 1994). It is expected that sands with large saturation gaps tend to favor fast infiltration of seawater into the beach. Indeed, McLachlan (1982) has observed a clear cycle of water exchange flux vs. tidal stage on a dissipative beach, which showed largest infiltration volumes of seawater on the late incoming tide, i.e., at the high tide position.

By trapezoidal integration of the water exchange fluxes at different tidal positions over the entire sandy beach (width ~110 m) near Weitou Bay, we derive a total water infiltration rate of $(0.089 + 0.109)/2 \times 55 + (0.109 + 0.035)/2 \times 55 \approx 9.2$ m^3 m^{-1} d^{-1}. Traditionally, the seawater infiltration rate through intertidal sandy beaches was estimated using hot thermistor probes to monitor interstitial flows. Several investigators have utilized this technique to measure seawater infiltration rates on a diversity of beaches in different regions. On an intermediate beach in North Carolina, Riedl (1971) estimated an average seawater infiltration rate of ~6 m^3 m^{-1} d^{-1}, and indicated that tides alone could account for about 25% of the total infiltration of seawater. McLachlan (1979) examined three high energy intermediate beaches in South Africa, and found that seawater infiltration rates ranged from 4 to 15 m^3 m^{-1} d^{-1}. McLachlan et al. (1985) investigated two reflective beaches with steep slope, coarse sand, and small tides near Perth, Australia. They identified high seawater infiltration rates of 19–92 m^3 m^{-1} d^{-1}. In comparison, dissipative flat beaches are more frequently characterized by low seawater infiltration rates. For instance, on two dissipative meso/-macrotidal beaches in Oregon, USA, seawater infiltration rates were found to range from 0.1 to 7 m^3 m^{-1} d^{-1} (McLachlan, 1989). In addition, the seawater infiltration rates were almost entirely accounted for by tidal effects, as most wave energy has been filtered out by the dissipative surf zones. Overall, our estimate derived from $^{224}Ra/^{228}Th$ disequilibria in the sediment falls in the range of seawater infiltration rates for intermediate beaches determined using the traditional hot thermistor probes.

4.3. Export fluxes of carbon and nutrients

Using the water exchange fluxes, we are able to calculate the residence time of porewater at different sampling sites. Our calculation shows that the porewater residence time (τ) in the upper 0–30 cm sand layer was 5.9 ± 0.3, 12.3 ± 0.5, and 62.6 ± 8.7 h at WTW-H, WTW-M, and WTW-L respectively, compared to an estimate of 12.2 ± 0.7 h for the upper 0–20 cm sand layer at the tidal flat in the German Wadden Sea (Table 5). Over the entire beach at Weitou Bay, the average porewater DIC addition (i.e., the DIC concentration difference between porewater and the overlying seawater) in the upper 0–30 cm sand layer was positively correlated with porewater residence time (Fig. 6). This correlation indicates that the production of DIC in porewater was a rate-limiting step for DIC export from the sandy beach into the sea. If we assume that there was no difference in the quality and quantity of TOC at different tidal positions, then the production of DIC in porewater over the entire beach at Weitou Bay may be simulated as a first-order kinetic reaction following the relation of

$$\frac{dc}{dt} = k(c_{eq} - c) \tag{6}$$

where c is DIC concentration in porewater, c_{eq} denotes the equilibrium concentration of DIC in porewater, and k is the rate constant for DIC production. Solving Eq. (6) with the boundary condition $c = c_0$, $t = 0$ gives the exact solution of

$$c\text{-}c_0 = (c_{eq} - c_0)(1 - e^{-kt}) \tag{7}$$

where c_0 refers to DIC concentration in the overlying seawater (~2110 μM). The best fit of Eq. (7) to the average DIC addition and porewater residence time data shown in Fig. 6 is obtained for the values $c_{eq} = 2952 \pm 88$ μM and $k = 0.078 \pm 0.021$ h^{-1}.

The cycling of carbon is tightly coupled with that of nitrogen. In conjunction with DIC production, ammonium (NH_4^+) is released into the ambient porewater as a result of the decomposition of organic matter in sandy sediments. In the highly oxic sand layer, it is nitrified rapidly to nitrite and subsequently to nitrate. This process is typically referred to as nitrification. With the evolution toward a more suboxic sand layer, nitrite and nitrate within the sediment may be utilized by denitrifying and anammox bacteria as electron acceptors, and be reduced to nitrous oxide (N_2O) and N_2 gases that can escape to the atmosphere. This process is known as denitrification. In the sandy seabed, denitrification is often coupled to nitrification. For

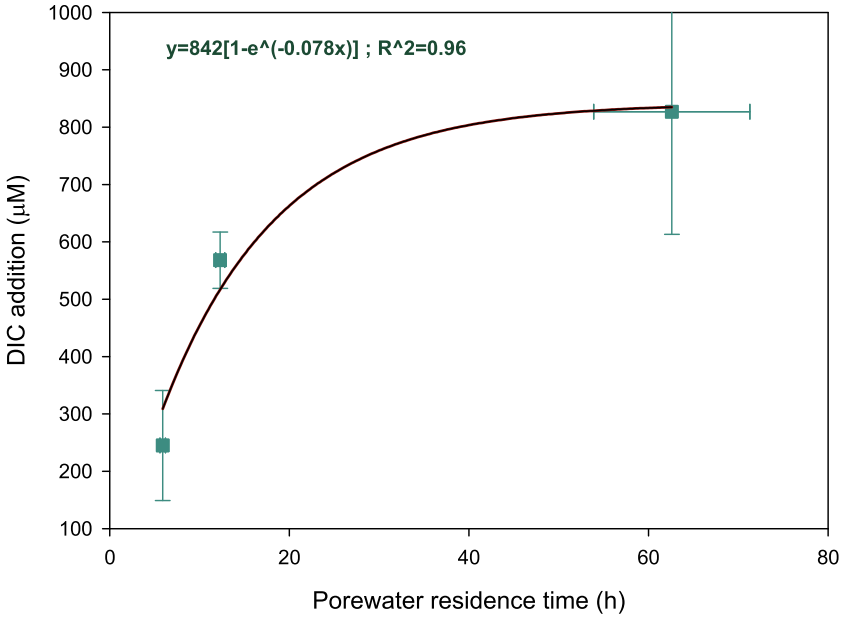

Fig. 6. Dependence of average DIC addition in porewater on the residence time of porewater within the intertidal sandy beach at Weitou Bay.

instance, Sundbäck et al. (2000) reported that nitrification within the sediment may contribute >85% of the nitrate required for the denitrification in North Sea sands. As it is expected that vigorous infiltration of seawater would increase the supply rate of dissolved oxygen into the sand, the pattern of interfacial water exchange flux across the investigated beach at Weitou Bay will facilitate a horizontal zonation of redox status. Indeed, at the high tide position (i.e., WTW-H) where the sand is most vigorously flushed, DIC and NO_3^- are added to the porewater at a rate very close to the Redfield C/N ratio of 106:16 (Fig. 7). This phenomenon can be interpreted as a result of the complete degradation of labile marine particles produced via photosynthesis in the water column. At the low tide position (i.e., WTW-L) where the redox condition evolves into a more suboxic state due to less efficient seawater infiltration, porewater C/N ratios are considerably higher than the Redfield ratio of 106:16. This scenario likely reflects nitrogen loss via denitrification in the sediment. In particular, denitrification appears to be tightly coupled to nitrification as evident

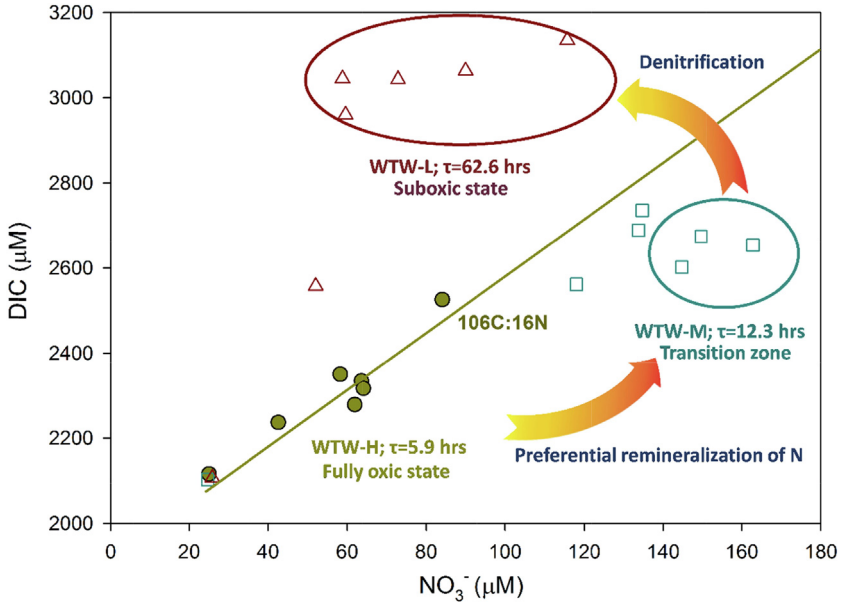

Fig. 7. A sketch depicting the evolution of the redox status within an intertidal sand system and its impact on the biogeochemical cycling of carbon and nitrogen in the sediment. Porewater data collected at WTW-H, WTW-M, and WTW-L are shown as filled yellow circles, open cyan squares, and open red triangles, respectively. (For interpretation of the references to color in this figure legend, the reader is referred to the web version of this article.)

from the enhanced nitrate concentration and the high level of nitrite in porewater (Table 3). Using the estimate of porewater residence time (62.6 h), we calculate a nitrogen loss rate of 3.3 mmolN m^{-2} d^{-1} at WTW-L. This value is similar in magnitude to the denitrification rates (~4.6 mmolN m^{-2} d^{-1}) determined in North Sea intertidal sands (Gao et al., 2010). At the mid-tide position (WTW-M) where the redox status lies within a transition zone between oxic and suboxic states, porewater C/N ratios are significantly lower than the Redfield ratio of 106:16. We ascribe this phenomenon to the preferential remineralization of N over C during the incomplete decomposition of marine particles, a mechanism commonly invoked to explain high C/N values relative to the Redfield ratio in marine sinking particles (e.g., Mayers, 1994).

As judged from the residence time of porewater (12.2 h), the redox condition of the upper 0–20 cm sand layer at the tidal flat in the German Wadden Sea very likely lies within a transition zone between oxic and suboxic states. At this location, the concentration level of NO_3^- in porewater is much elevated in comparison to that in seawater (Table 4). While the concentration of NH_4^+ is relatively high, porewater NO_2^- is generally close to the detection limit of the analytical method, suggesting that denitrification might be insignificant at this sampling site. By assuming that DIC and DIN are released to the porewater at a rate similar to that found at WTW-M, i.e., 106:22 (Fig. 7), we estimate an average addition of ~940 μM DIC into the porewater, or an equivalent DIC concentration of ~3100 μM. This estimate is in general agreement with historical measurements of porewater DIC at the tidal sand flat in the German Wadden Sea (Billerbeck et al., 2006).

Export fluxes of DIC and nutrients from the two intertidal sand systems can be obtained using a relation similar to Eq. (4). By multiplying the concentration difference between porewater and the overlying seawater by the seawater infiltrate rate, and subsequently integrating the products from the beach surface (z = 0) to the sampling depth (z = 20–35 cm), we derive DIC export fluxes of 21.8 ± 1.0, 65.9 ± 2.6, and 20.1 ± 4.4 mmolC m^{-2} d^{-1} for WTW-H, WTW-M, and WTW-L, respectively. In comparison, DIC export flux from the tidal sand flat in the German Wadden Sea was 89.4 ± 6.0 mmolC m^{-2} d^{-1} (Table 5). Accordingly, DIN export fluxes are estimated to be 3.6 ± 0.2, 13.7 ± 0.6, 0.8 ± 0.2, and 18.6 ± 1.2 mmolN m^{-2} d^{-1}, respectively. Overall, our estimates of DIC export flux are similar in magnitude to the respiration rates of 10–283 mmolC m^{-2} d^{-1} determined in coastal sands using a noninvasive eddy correlation technique (e.g., Huettel et al., 2014). They are also comparable to the benthic fluxes of DIC determined in organic rich estuarine sediments using the $^{224}Ra/^{228}Th$ disequilibrium method (e.g., Cai et al., 2015). In a way similar to the calculation of total seawater infiltration rate, we integrate the DIC flux values at different tidal positions over the entire sandy beach at Weitou Bay, and derive a total DIC export flux of 4.8 molC m^{-1} d^{-1}. Based on the measurements of TOC content in the sand (Table 1), we calculate TOC stock at the respective tide positions across the sandy beach at Weitou Bay. Dividing TOC stock by the benthic flux of DIC gives carbon turnover rates of 490, 220, and 730 d for WTW-H, WTW-M, and WTW-L, respectively (Table 5). The result suggests that without an extrinsic source, TOC in the sand would be exhausted within 1–2 years. This scenario, however, does not happen in the real world. On the contrary, it has been thought that sandy beaches are in equilibrium with organic inputs from the ocean (e.g., McLachlan and Turner, 1994). Previous studies revealed that fresh organic matter filtered into the sands and benthic primary production are the main mechanisms that maintain the DIC export from coastal sands. By assuming that our estimates of DIC export flux derived from this study are typical for the permeable sand beds in the continental shelves, we extrapolate an average DIC export flux of 49.3 mmolC m^{-2} d^{-1} to the global continental shelf area covered by sandy sediments (~9.6×10^6 km^2), and obtain a total respiration rate of ~172 TmolC y^{-1}. Provided with an estimate of ~920 TmolC y^{-1} for global shelf primary production (Liu et al., 2010), this simple extrapolation indicates that ~19% of total organic matter produced via photosynthesis in the water column is effectively recycled in the sand beds. Overall, our estimate is higher than the upper bound of the previous values obtained by Huettel et al. (2014), who reported that a fraction of ~4–13% of water column primary production was regenerated in permeable sandy sediments. In this respect, our study suggests that intertidal sand systems can be envisaged as a "digestive system" of biogenic particles in the ocean.

5. CONCLUDING REMARKS

The use of $^{224}Ra/^{228}Th$ disequilibria as a proxy for solute exchange across the sediment-water interface began with the work of Cai et al. (2012). Ever since then, this proxy has been expanded considerably to examine interfacial fluid transport mechanisms and to quantify benthic fluxes of a variety of dissolved constituents (e.g., Cai et al., 2014, 2015; Hong et al., 2017, 2018; Shi et al., 2018, 2019). Nonetheless, up to now the application of this proxy is confined mostly to muddy, cohesive sediments where bio-irrigation governs fluid transport across the sediment-water interface. In this scenario, solute exchange is visualized to take place at a highly perforated interface in which molecular diffusion becomes quantitatively more important than turbulence in bringing about the transfer of dissolved constituents. Here we propose an alternative scheme for the use of $^{224}Ra/^{228}Th$ disequilibria to examine solute transfer in a permeable sandy seabed where owing to the high permeability of the sandy sediment, advective flows control solute transport across the sediment-water interface. A case study was carried out in two different intertidal sand systems that are subject to periodic tidal inundation and swash actions. With the aid of a simple two-dimensional advective cycling model, we demonstrate that there is a general trend of seaward decrease in the interfacial water exchange flux over the sandy beach. This fluid transport pattern facilitates a horizontal zonation of redox condition in the sediment, which appears to exert profound impacts on the carbon and nutrient dynamics within the intertidal sand system. Furthermore, we show that export fluxes of DIC and DIN from an intertidal sand system,

which were traditionally thought to be low because of low organic carbon contents therein, can rival those from organic rich estuarine sediments. From this perspective, our study suggests that the role of sandy sediments in the biogeochemical cycling of carbon and nutrients needs to be revisited.

Declaration of Competing Interest

The authors declare that they have no known competing financial interests or personal relationships that could have appeared to influence the work reported in this paper.

ACKNOWLEDGEMENTS

This work was supported by the National Major Scientific Research Project of China through Grants No. 2016YFC0300709, and by the Natural Science Foundation of China (NSFC) through Grants No. 41776083. We thank the Nationalparkverwaltung Niedersaechsisches Wattenmeer for permission to access the site near Sahlenburg for our study. PC acknowledges the Alexander von Humboldt Foundation for her generous support of a research stay in Alfred-Wegener Institute for Polar and Marine Research, Germany. The authors thank Ms. Pingping Mi for the logistic support of this research.

REFERENCES

Aller R. C. (1980) Quantifying solute distributions in the bioturbated zone of marine sediments by defining an average microenvironment. *Geochim. Cosmochim. Acta* **44**, 1955–1965.

Anschutz P., Smith T., Mouret A., Deborde J., Bujan S., Poirier D. and Lecroart P. (2009) Tidal sands as biogeochemical reactors. *Estuar. Coast. Shelf Sci.* **84**, 84–90.

Berg P., Long M. H., Huettel M., Rheuban J. E. and McGlathery K. J., et al. (2013) Eddy correlation measurements of oxygen fluxes in permeable sediments exposed to varying current flow and light. *Limnol. Oceanogr.* **58**, 1329–1343.

Billerbeck M., Werner U., Polerecky L., Walpersdorf E., deBeer D. and Huettel M. (2006) Surficial and deep pore water circulation governs spatial and temporal scales of nutrient recycling in intertidal sand flat sediment. *Mar. Ecol. Prog. Ser.* **326**, 61–76.

Cai W.-J., Dai M., Wang Y., Zhai W., Huang T., Chen S., Zhang F., Chen Z. and Wang Z. (2004) The biogeochemistry of inorganic carbon and nutrients in the Pearl River estuary and the adjacent Northern South China Sea. *Cont. Shelf Res.* **24**, 1301–1319.

Cai P., Shi X., Moore W. S. and Dai M. (2012) Measurement of Ra-224:Th-228 disequilibrium in coastal sediments using a delayed coincidence counter. *Mar. Chem.* **138**, 1–6.

Cai P., Shi X., Moore W. S., Peng S., Wang G. and Dai M. (2014) ^{224}Ra:^{228}Th disequilibrium in coastal sediments: Implications for solute transfer across the sediment-water interface. *Geochim. Cosmochim. Acta* **125**, 68–84.

Cai P., Shi X., Hong Q., Li Q., Liu L., Guo X. and Dai M. (2015) Using ^{224}Ra/^{228}Th disequilibrium to quantify benthic fluxes of dissolved inorganic carbon and nutrients into the Pearl River Estuary. *Geochim. Cosmochim. Acta* **170**, 188–203.

Cook P. G., Rodellas V., Andrisoa A. and Stieglitz T. C. (2018) Exchange across the sediment-water interface quantified from porewater radon profiles. *J. Hydrol.* **559**, 873–883.

Dai M., Wang L., Zhai W., Li Q., He B. and Kao S.-J. (2008) Nitrification and inorganic nitrogen distribution in a large perturbed river/estuarine system: the Pearl River Estuary, China. *Biogeosciences* **5**, 1227–1244.

Gao H., Schreiber F., Collins G., Jensen M. M. and Kostka J. E., et al. (2010) Aerobic denitrification in permeable Wadden Sea sediments. *ISME J.* **4**, 417–426.

Hong Q., Cai P., Shi X., Li Q. and Wang G. (2017) Solute transport into the Jiulong River estuary via pore water exchange and submarine groundwater discharge: New insights from ^{224}Ra/^{228}Th disequilibrium. *Geochim. Cosmochim. Acta* **198**, 338–359.

Hong Q., Cai P., Geibert W., Cao Z., Stimac I., Liu L. and Li Q. (2018) Benthic fluxes of metals into the Pearl River Estuary based on ^{224}Ra/^{228}Th disequilibrium: From alkaline earth (Ba) to redox sensitive elements (U, Mn, Fe). *Geochim. Cosmochim. Acta* **237**, 223–239.

Huettel M., Ziebis W. and Forster S. (1996) Flow-induced uptake of particulate matter in permeable sediments. *Limnol. Oceanogr.* **41**, 309–322.

Huettel M., Ziebis W., Forster S. and Luther G. W. (1998) Advective transport affecting metal and nutrient distributions and interfacial fluxes in permeable sediments. *Geochim. Cosmochim. Acta* **62**, 613–631.

Huettel M., Berg P. and Kostka J. E. (2014) Benthic exchange and biogeochemical cycling in permeable sediments. *Annu. Rev. Mar. Sci.* **6**, 23–51.

Liu, K.-K., Atkinson, L., Quinones, R. and Talaue-McManus, L. (eds.) (2010) *Carbon and nutrient fluxes in continental margins-A global synthesis*. Springer-Verlag, Berlin, Heidelberg.

Mayers P. A. (1994) Preservation of elemental and isotopic source identification of sedimentary organic matter. *Chem. Geol.* **114**, 289–302.

Mclachlan A. (1979) Volumes of seawater filtered by eastern Cape sandy beaches. *S. Afr. J. Sci.* **75**, 75–79.

Mclachlan A. (1982) A model for the estimation of water filtration and nutrient regeneration by exposed sandy beaches. *Mar. Environm. Res.* **6**, 37–47.

Mclachlan A., Eliot I. G. and Clarke D. J. (1985) Water filtration through reflective microtidal beaches and shallow sublittoral sands and its implications for an inshore ecosystem in Western Australia. *Estuar. Coast. Shelf Sci.* **21**, 91–104.

Mclachlan A. (1989) Water filtration by dissipative beaches. *Limnol. Oceanogr.* **34**, 774–780.

Mclachlan A. and Turner I. (1994) The interstitial environment of sandy beaches. *Mar. Ecol.* **15**, 177–211.

Moore W. S. and Arnold R. (1996) Measurement of ^{223}Ra and ^{224}Ra in coastal waters using a delayed coincidence counter. *J. Geophys. Res.* **101**, 1321–1329.

Riedl R. J. (1971) How much seawater passes through sandy beaches? *Int. Rev. Pes. Hydrobiol.* **56**, 923–946.

Riedl R. J., Huang N. and Machan R. (1972) The subtidal pump: a mechanism of water exchange by wave action. *Mar. Biol.* **13**, 210–221.

Santos I. R., Eyre B. D. and Huettel M. (2012) The driving forces of porewater and groundwater flow in permeable coastal sediments: A review. *Estuar. Coast. Shelf Sci.* **98**, 1–15.

Sundbäck K., Miles A. and Goransson E. (2000) Nitrogen fluxes, denitrification and the role of microphytobenthos in microtidal shallow-water sediments: an annual study. *Mar. Ecol. Prog. Ser.* **200**, 59–76.

Shi X., Mason R. P., Charette M. A., Mazrui N. M. and Cai P. (2018) Mercury flux from salt marsh sediments: Insights from a comparison between ^{224}Ra/^{228}Th disequilibrium and core incubation methods. *Geochim. Cosmochim. Acta* **222**, 569–583.

Shi X., Wei L., Hong Q., Liu L., Wang Y., Shi Xueyin, Ye Yin and Cai Pingh (2019) Large benthic fluxes of dissolved iron in China

coastal seas revealed by $^{224}Ra/^{228}Th$ disequilibria. *Geochim. Cosmochim. Acta* **260**, 49–60.

Tamborski J., Beek P., Rodellas V., Monnin C., Bergsma E., Stieglitz T., Heilbrun C., Cochran J. K., Charbonnier C., Anschutz P., Bejannin S. and Beck A. (2019) Temporal variability of lagoon–sea water exchange and seawater circulation through a Mediterranean barrier beach. *Limnol. Oceanogr.* **64**, 2059–2080.

Associate editor: Franco Marcantonio